

Infrared in-line monitoring of flaws in steel welded joints: a preliminary approach with SMAW and GMAW processes

Original

Infrared in-line monitoring of flaws in steel welded joints: a preliminary approach with SMAW and GMAW processes / Santoro, Luca; Sesana, Raffaella; Molica Nardo, Rosario; Cura, Francesca Maria. - In: INTERNATIONAL JOURNAL, ADVANCED MANUFACTURING TECHNOLOGY. - ISSN 0268-3768. - (2023), pp. 2655-2670. [10.1007/s00170-023-12044-2]

Availability:

This version is available at: 11583/2981007 since: 2023-08-09T09:27:43Z

Publisher:

Springer Nature

Published

DOI:10.1007/s00170-023-12044-2

Terms of use:

This article is made available under terms and conditions as specified in the corresponding bibliographic description in the repository

Publisher copyright

(Article begins on next page)



Infrared in-line monitoring of flaws in steel welded joints: a preliminary approach with SMAW and GMAW processes

Luca Santoro¹ · Raffaella Sesana¹ · Rosario Molica Nardo² · Francesca Curá¹

Received: 13 April 2023 / Accepted: 21 July 2023 / Published online: 9 August 2023
© The Author(s) 2023

Abstract

The non-destructive full-field non-contact thermographic technique is applied for non-destructive flaw detection of the welded joints, in real-time and offline configuration. In this paper, a thermographic procedure for real-time flaw detection in manual arc welding process is presented. Surface temperature acquisitions by means of an IR camera were performed during arc welding process of 8 specimen both for calibration and validation of the numerical model. The investigated variables are the technique (manual stick arc (SMAW) and gas arc (GMAW) welding) and the joint shape (butt and T joint) for steel joints, in sound conditions and with artificial flaws. Numerical simulation of welding thermal transients was run to obtain the expected surface temperature fields and thermal behavior for different welding parameter configurations. Hardness measurement and micro-graphic analysis were performed to validate numerical simulation results. The real-time thermographic study of the weld pool gives direct indications of anomalies; local studies of the thermal transient and thermal profiles can detect some kind of flaws; microstructural analysis of Heat-Affected Zone (HAZ) and surrounding areas highlights the presence of austenite and martensite distribution which justifies the thermal transients and thermal profiles for different welding configurations. Comparing real-time IR acquisition of the welding process with simulated thermal contours of sound processes provides information of presence of some kind of flaws. Since most of the flaws are generated in the weld pool, it is possible to recognize anomalies directly from the thermal acquisitions or with post-processing the acquired data.

Keywords Process monitoring · Infrared thermography · Non-contact · Porosity · Welding · Simulation · Real-time

1 Introduction

In the field of manufacturing, the integrity of welded joints is paramount to the overall structural stability and performance of the final product. Many factors can affect the welding

properties and generate flaws, for example, a wrong choice of weld parameters, a non-correct preparation, and cleaning of the weld grooves as discussed in [1–3]. Any flaws or defects in these joints, even microscopic ones, can significantly affect their mechanical properties, leading to potential failures under stress or cyclic loading. The real-time detection of such defects during the welding process is crucial for two main reasons. Firstly, it allows for immediate corrective action, reducing the need for costly and time-consuming post-production inspections and rework. Secondly, it can significantly enhance the overall quality and reliability of the welded joints, thereby extending the lifespan of the final product. However, current defect detection methods often fall short in terms of speed, accuracy, and ability to detect certain types of defects.

As regards non-destructive testing (NDT) techniques, they are widely employed in industries to detect and evaluate defects in materials without causing damage. Common NDT methods include visual inspection, ultrasonic testing, magnetic particle testing, liquid penetrant testing, and

All authors are contributed equally to this work.

✉ Luca Santoro
luca.santoro@polito.it
Raffaella Sesana
raffaella.sesana@polito.it
Rosario Molica Nardo
rosario.molicanardo@adesndt.com
Francesca Curá
francesca.cura@polito.it

¹ DIMEAS, Politecnico di Torino, Corso Duca degli Abruzzi 24, Torino, TO 10129, Italy

² ADES Group, Via della Pentapoli 48, Priolo Gargallo, SR 96010, Italy

radiographic testing. However, each of these methods has limitations. Visual inspection, while straightforward and cost-effective, can only detect surface defects and is highly dependent on the inspector's experience. Ultrasonic testing and radiographic testing, though capable of detecting subsurface defects, require complex equipment and skilled operators and may not be suitable for complex geometries or certain material types. Magnetic particle testing and liquid penetrant testing, on the other hand, are limited to detecting surface and near-surface defects. Moreover, most of these techniques are time-consuming and not suitable for real-time monitoring during the welding process. Therefore, there is a pressing need for a more efficient and effective real-time defect detection method, which is the primary motivation for the research presented in this paper.

As for the choice of Shielded Metal Arc Welding (SMAW) and Gas Metal Arc Welding (GMAW) processes, as well as the specific joint shapes studied in this research, were chosen for scientific purposes. These welding processes and joint shapes are among the most commonly used in various industrial applications, including automotive, shipbuilding, and construction. Therefore, improving the defect detection in these specific scenarios can have a broad and significant impact on these industries. For instance, in the automotive industry, a flawed weld could lead to critical failures in vehicle components, posing safety risks. By focusing on SMAW and GMAW processes and commonly used joint shapes, this research aims to address a real and pressing issue in the manufacturing sector, making it highly relevant and valuable to both academia and industry.

The mechanisms which lead to the formation of flaws are several; [4] offer an extensive review on the mechanisms behind porosity generation in aluminum welded joints. Their study provides valuable insights that can enhance our understanding of pore formation phenomena and help anticipate what to expect in such processes.

In his work, [5] presents the effect of arc instability in defect formation of pipes welding; in the results, a topographic map is presented, correlating flaws to the arc interruption zone. A strong relation between molten pool dynamic phenomena and anomalies presence in the weld bead is highlighted; as an example, the topography in [5] is the result of an unstable solidification of the weld pool. The study of [6] proposes a visual sensing algorithm applied to images of the weld bead applied to the climbing helium arc welding process; again, there is some relation between the melt pool solidification and defect creation. In [7], another study on weld pool dynamics and flaws is presented, where by analyzing the molten flows it is possible to retrieve bead dimension, lack of penetration, burn trough, and humping. Most of the flaws originate in the weld pool (pores, hot cracks) or in its proximity due to the multiple physical and chemical processes taking place, as shown in [1]. In fact,

discontinuities in the process introduced by an irregular arc, improper preparation of the welding groove (bad milling, contaminated surface), an improper pre-post heat treatment, or more in general by a non-correct process parameter setup, lead to defect formation [8]. In the industrial approach, it is common use to check the quality of a joint by means of non-destructive tests at different processing steps. Aucott et al. [9] presents an online radiography study to hot crack formation. Notably, the works [10–12] have provided valuable insights into the metallurgical behavior of various claddings, the influence of torch oscillation on microstructure, and the potential for real-time defect detection.

Indeed, while it is undeniable that a considerable multitude of imperfections in the welding process originates from the welding pool, it is also crucial to bear in mind that specific materials can manifest cracks within the Heat-Affected Zone (HAZ). However, for the purposes of this preliminary study, our focus was primarily on the welding pool, as it typically contains the majority of the information relevant to our investigation. Consequently, conducting experimental surveillance of the welding pool, alongside meticulous scrutiny of the HAZ in future studies, can furnish invaluable insights into the intricate mechanisms that give rise to these defects. The dynamic is fast, and it develops at high temperatures, then thermal monitoring systems appear to be the best suited for real-time monitoring. Within the literature, a significant number of researchers have devoted their efforts to the exploration and understanding of thermographic testing and monitoring methodologies. Thermography, a non-contact technique, enables the acquisition of thermal maps of a component's surface over a designated observational period. In its most recent applications, an innovative approach known as active or stimulated thermography has emerged, yielding promising results.

However, it is essential to acknowledge that thermography, akin to any other technique, possesses its unique set of advantages and disadvantages. On the one hand, the non-invasive nature of thermography, coupled with its capacity to provide real-time, continuous monitoring of a process, renders it particularly suitable for applications such as welding, where conditions are subject to rapid fluctuations. Moreover, its ability to encompass extensive areas in a single scan enhances its efficiency in detecting anomalies. On the contrary, the reliability of thermography can be influenced by environmental variables such as ambient temperature and material emissivity, potentially compromising the accuracy of the readings. Furthermore, thermography primarily measures surface temperature and may not accurately represent conditions beneath the surface. Additionally, the interpretation of thermographic data can prove to be complex, necessitating the use of sophisticated software and skilled operators. Despite these challenges, the potential of thermography in applications such as real-time monitor-

ing of welding processes is substantial and merits further investigation.

Active thermography is a diagnostic tool that thermally stimulates a component by means of an external heat source in order to characterize thermal properties and/or detect flaws. What is known from this methodology is that the thermal response of a volume of a component with a defect is different than in sound regions. Thermal stimulation can be classified into two categories: photo-thermal stimulation, which introduces the heat through the surface, and volumetric stimulation, where the heat is produced in the bulk of the material by dissipative phenomena. This technique well adapts to the offline investigation of welding micro/structure and defect detection, and it is widely applied for composites and laminates [13–15]. In [16], for example, an ultrasound stimulation is used to heat up the component in order to detect cracks. Similarly, [17] uses ultrasound thermography for microcracks detection in dissimilar metal welds. Active thermography is not used only for defect detection but can also give important information about the welded area; in [18], laser stimulation is used in order to measure the welded area in resistance projection welding. In [19], the same stimulation is used to assess the microstructural properties of a heat-treated steel. Another volumetric stimulation is electromagnetic induction; in [20], an induction system is used to heat a stainless steel weld. [21] proposes induction thermography for condition monitoring of overlay welded components under multi-degradation; one of the main advantages of this technique is that, with proper signal processing, it can give a visual indication of anomalies. In [22], laser, induction, and heat gun stimulation are used to detect defects in nickel superalloy welds. In [23], a crack detection method is proposed; the method uses a laser stimulation, but it can detect only surface cracks; the same method is used in [24] with except to an additional post-processing using the second temporal derivative in order to mark the crack in the image. The laser is also used in [25] to assess the nugget extensions in the spot-welded joint. Similarly, active thermography using both laser and lamp stimulation is used on Cu solder connections [26].

A more traditional approach is represented by passive thermography, a technique in which the thermal response of the material is generated by mechanical stimulation (for example, fatigue loads). This excitation generates dissipative phenomena, and their thermal effects on the component surface are acquired and processed. This technique was successfully applied for progressive damage detection in case of mechanical fatigue in elastic and plastic field [27, 28], for fatigue resistance assessment [29, 30]. Another interesting application is the real-time welding process monitoring. Nowadays, the in-line acquisition of thermal mapping of the process has been applied to evaluate macroscopic properties of the joint, for example, hardness and tensile resistance [31].

Some further experiments to detect defects with non-contact automated methods are reported in the literature. Most of the literature focuses on electric data monitoring and processing; [32] studies the correlation between arc voltage and current signal, light signal, and weld quality in plasma-arc welding. [32] presents two algorithms that can detect three phases of the plasma-arc (non-penetration, transition, keyhole). A more classical non-destructive testing method is ultrasonic testing; in [33], an in-process automated non-destructive evaluation is proposed. In [34], an overview of the monitoring method of laser and laser-arc hybrid welding processes is reported; it is evident that many methods can be automatized, and light-based monitoring of weld pool is giving promising results. In [35], the possibility to detect and quantify the lack of penetration in laser-arc hybrid welding is investigated by means of a light-based method that correlates the key-hole area and the arc area to the penetration state. In [35], it is demonstrated that with the use of a high-speed camera, it is possible, with proper calibration, to detect anomalies in penetration depth with 98% reliability, which makes this procedure a possible candidate for reliable real-time defect detection in laser-arc hybrid welding. In [36], a light-based sensing technology for aluminum automated real-time subsurface defect detection in the welding process is proposed. The methodology implements spectrometric analysis and signal processing. Machine learning systems are required for reliable porosity detection. The prediction model shows an identification accuracy of 95% at a fast learning speed. Unfortunately, in the paper, no information is given on the sensitivity of the methodology with respect to the pore dimension and position. The defect in the weld bead introduces a discontinuity in thermal transient related to the process heat source (weld torch). Infrared acquisitions allow to detect the actual weld pool thermal contour during solidification. The welding pool temperature is correlated to weld penetration depth [37]. In [38], this aspect is investigated to propose a real-time detection procedure based on a surface thermal acquisition of the welding pool. In particular, the IR monitoring welding pool temperature and corresponding welding penetration for varying welding currents in the tungsten arc process applied to SAE steel are studied. The used sensor is a pyrometer, acquiring point temperature in the welding pool. A critical issue in this procedure consists in the fact that a pyrometer has to be carefully positioned to reliably acquire the welding pool temperature. A simple thermal data signal processing procedure, based on two filterings, is implemented to set a threshold signal value above which the possible defect is detected. In the same investigation, some concentrated artificial defects are introduced and detected by the thermal acquisition. In particular, two microinclusions and water spraying. The perturbation in thermal contours in cooling profiles allowed to detect sub-superficial defects. No sensitivity analysis is performed on defect dimension and position. As an evolution of [38], in

[39], a study of the optimal offset distance between IR sensor (pyrometer) and welding torch is presented, to calibrate a procedure for detecting the welding quality. The idea is that the thermal cooling transient can be related to welding quality, and a difference in local temperature at given distances from the welding torch can result from a non-standard welding process. The used sensor is again a pirometer, and the procedure is proposed for real-time quality detection. No investigation is done on superficial and sub superficial defects. In [31], the thermographic acquisition of a single pass plasma weld is used to correlate the tensile strength of the weld joint and the micro-hardness to the cooling rate for stainless steel. In particular, the cooling rate between 800 and 500 °C of points acquired on the welding line is the parameter used to correlate with the tensile and hardness properties of the welding. This investigation [37] is based on the assumption that the welding microstructure influences mechanical properties and it is affected by the cooling process. The high-speed IR camera is used to detect the points on the welding surface where the temperature is more elevated than in the welding pool. As regards the thermal simulation of the process, different approaches have been explored. In fact, some engineers prefer to simulate the joint global thermal behavior, introducing a thermal source and the fill material to simulate the thermal process along the path and predict the cooling curves, micro-structures, and distortions. Others prefer a more accurate analysis considering fluid dynamics and electrical and metallurgical phenomena. In [40], a thermal measurement of a laser welding of a polymer is presented; this work uses a *COMSOL Multiphysics* Software numerical thermal simulation in order to validate the thermal data.

In [41], an aluminum T joint is investigated. In particular, thermographic acquisition on the surface opposite to the welded one is performed in two welding conditions. The acquired surface is coated with graphite to maximize thermal emission. Thermal data and micrographic images are used to calibrate a numerical finite element model with the aim of estimating the thermal field and comparing the two welding processes. The simulation is carried out by means of *COMSOL Multiphysics* Software. In [42], the simulation has been done with the research software *Flow 3D*; it was possible to simulate the free flow of the droplet and weld pool moving along the weld path. This approach gives the possibility to have an indication of the thermal behavior of the joining; in particular, it provides accurate information about the influence of the groove shape on the melt pool sustain and heat evacuation ability. The same approach is used in [43] where is presented a numerical simulation of defect formation in narrow gap GMAW of 5083 Al-alloy; in this work, the software used is again *Flow 3D*. Similarly, [44] present an example that includes an arc heat flux model, an arc pressure model, and an electromagnetic force (EMF) model.

Other researchers focus on the thermal transient phenomena, without considering fluid dynamic and electrical phenomena. In [45], the author uses the software *MSC-MARC-MENTAT* when modeling the welding process by means of a thermo-mechanical simulation which permits to accurately calculate thermal behavior of the joining process thanks to the use of a moving thermal source, this approach is computationally lighter and easier to validate. Sebayang et al. [45] shows how it is possible to predict phase fraction in multiphase material, such as steel, thanks to thermal cooling transient simulation results and the PLOTV subroutine of *MSC-MARC*. Similarly, in [46], a simulation in *MSC-MARC-MENTAT* is performed in order to predict distortions in wire arc additive manufacturing. An overview of thermal source models is presented in [47]; the most used for arc welding application is the so-called *Goldak model*. In [48], a laser-MIG hybrid arc brazing-fusion welding of Al alloy to galvanized steel simulation is presented. [48] uses *ANSYS* to simulate the thermal transient induced by the two heat sources, laser beam and electric arc, and influenced by the dissimilar metals which takes part in the process. The objective of this work is to propose a procedure for subsurface defect detection by means of the real-time passive thermographic analysis of welding process of steel laminates. In particular, lack of penetration, suction pores, spatter, and burn throughs were artificially induced in welded joints. To this aim, FEA simulations of the thermal transient of the process and of the resulting microstructure and extension of the HAZ were performed, and then an experimental validation followed.

2 Materials and methods

This works aims at presenting a preliminary approach for infrared real-time monitoring of flaws in the welding process of steel joints. In particular, the investigation focused on the SMAW and GMAW processes. Two simple case studies were selected, a butt joint and a tee joint. The base material is an S275JR steel plate 5 mm thick, of which chemical composition is reported in Table 1.

By means of the Graville Weldability Diagram [49], it is possible to calculate the Carbon Equivalent *CE* of the alloy by the formula:

$$CE = C + \frac{Mn}{6} + \frac{Cr + Mo + V}{5} + \frac{Ni + Cu}{15} = 0.5 \quad (1)$$

Table 1 Chemical composition (%wt) of S275JR steel

C%	Mn%	P%	S%	N%	Cu%
0.21	1.5	0.035	0.035	0.012	0.55

Table 2 Optimal welding parameter

	Voltage	Current	Power	Travel speed	Heat input
SMAW	18V	95A	1700W	2 mm/s	850J/mm
GMAW	25V	50A	1250W	2 mm/s	625J/mm

where each element symbols indicates the percent quantity of the indicated element. The *CE* value indicates that, depending on condition, this steel may suffer of HAZ cracking.

2.1 Experimental method

The welding system is *TECNOWELD MIG 110, 35-100 A, 0.6–0.8 mm* and *AWELCO ARC 250*, while the consumable used for SMAW technique is *Oerlikon TENAX 35 S* of $\phi = 2\text{mm}$.

The sound welding joint was obtained by means of setting the optimal welding parameter presented in Table 2 for the two techniques.

In particular, artificial flaws were obtained by running intentionally wrong welding parameters and/or practices, focusing on lack of penetration, suction pores, spatter, and breakthroughs.

Subsuperficial flaws detection is presented in this paper. In particular, several suction pores with average dimensions of 2 mm are investigated. Furthermore, several spatters were identified. Then, by visual inspection of the joint, the areas to be investigated were chosen. In Fig. 1, a butt joint specimen is shown, and some reference marks are reported on the specimen in order to perform the spatial calibration in the thermal contours and time-temperature plots.

The thermal acquisition system utilized in this research is a Flir A40, equipped with a $24^\circ \times 18^\circ$ lens; the calculated value for the fields of view are presented in Table 3. This system is capable of measuring a temperature range spanning from 300 to 2000 °C. The system is positioned at a fixed distance of 1.00m from the specimen, ensuring consistent measurements. The thermal sensitivity of the system is 0.08 °C at 30 °C. The spectral range of the system, an important factor in thermal imaging, extends from 7.5 to 13 micrometers.

**Fig. 1** Butt joint specimen

The accuracy of the system, quantified as a percentage of the reading, is within a margin of $\pm 2\%$. This level of precision underscores the reliability of the Flir A40 in conducting thermal measurements for this study. For the butt joint welds, the specimens were meticulously oriented to ensure an angle of less than 5 degrees relative to the camera. In the case of the tee joint specimens, the camera was strategically aligned with the bisector of the tee joint. The camera was centrally positioned along the weld path, a setup that ensured all specimens were encompassed within the frame. This careful positioning of the camera and specimens was crucial to the accuracy and consistency of the thermal measurements. The thermal data are post-processed with *FLIR ResearchIR*.

In literature and in experience, it is reported that the surface's thermal emissivity changes strongly with temperature. The phenomenon observed in the present research (heating, fusion, solidification, cooling) involves a wide range of temperatures. Many researchers over the years tried to overcome this problem. In [50], the author presents a study on emissivity variations with temperature in metals and proposes a method for assessing it by means of a pyrometer. A similar approach was applied in the present work. In particular, emissivity was set as follows. Observing the time-temperature plot at several points on the surface, it is possible to recognize an isothermal interval corresponding to the phase transition between the liquid and solid state of the welding material. This interval temperature corresponds, for S275JR steel, to in the range 1480–1526 °C [51], and then the emissivity was calibrated according to this set point, that is, 0.85 for SMAW technique and 0.35 for GMAW technique. As a cross-check, the welding current intensity was acquired by means of an amperometer. As regards the thermal post-processing analysis, 3 different types of curves were monitored and processed. The first kind of curve (C1) consists in the heating and cooling curves (time plots) of single points positioned on the axis of the welding; the time plots were extracted from the thermal acquisition. The selected points were represented by a 3pixel x 3pixel ROI in the center of the weld path. In particular, points corresponding to sound and defective areas were acquired. The second kind of curve (C2) consists in

Table 3 IR camera acquisition parameters

HFOV	VFOV	IFOV
0.51m	0.38	1.59m

the temperature profile of the whole welding line in a given time instant, that is, the temperature profile along the weld path. Last, the third kind of curve (C3) is represented by the temperature profile of a line perpendicular to the weld path in the time instant corresponding to the temperature peak in the welding point for sound and defective welding areas. A micrographic analysis of welding cross-section, by means of *Nital 3%* chemical etching, was run with two aims. The first aim is to calibrate the numerical model which, as in paragraph 3.2 will be explained, involves microstructure aspects. The second aim is to cross-check that the welding process was correctly run. To this aim, microhardness measurements were run by means of *microvickers knoop innovatest nova 130*, according to [52].

2.2 FEM simulation

Within the scope of defect detection, establishing a definitive threshold using the experimental curve presents a significant challenge due to the potential for unusual or unexpected behavior. However, this obstacle can be addressed through the implementation of a numerical simulation. The simulation is designed to define what we refer to as the “sound” parameter. This parameter is integral to the process of defect detection, as it allows for the differentiation between the thermal transients associated with defects and those consistent with a defect-free or “sound” region. This distinction is crucial in enhancing the accuracy and reliability of real-time defect detection during the welding process.

Central to our approach is the development of a numerical model designed to simulate the thermal behavior of defect-free welding. This model focuses on the generation of corresponding C1, C2, and C3 profiles under various welding parameter settings. The validity of these simulated profiles is then established by comparing them with the experimental profiles obtained from sound welding conducted under the same parameter settings. Once validated, these simulated curves serve as a benchmark for comparison with actual experimental curves, thereby enabling the assessment of defect presence.

For the initial phase of this study, simulations were exclusively conducted on Shielded Metal Arc Welding (SMAW) butt weldings. This decision was driven by the fact that the experimental validation of our preliminary investigation proved to be more reliable in this configuration. The surfaces acquired in this setup are perpendicular to the infrared (IR) sensor, ensuring that the thermal emissions are not influenced by acquisition angles. While the current results are specific to SMAW butt weldings, our future work will extend this methodology to T joint configurations and Gas Metal Arc Welding (GMAW) processes.

The CAD of the butt weld piece was modeled on *Solidworks 2021*; it is composed of an assembly of three bodies: 2

symmetrical plates of dimensions 500x125x5mm with a 20° V-shaped weld groove and the weld fill which is defined as the group of elements of the whole filler contact body. The elements of the filler, before being activated by the moving thermal flux’s volume, were set with mechanical and thermal scaled properties (Marc’s option *quiet*), by a factor 10^{-5} . The simulation was performed on *MSC Marc Mentat 2021* software. The model is composed of 39,316 nodes and 123,620 Tetra4 elements (linear tetrahedral elements). In Fig. 2, an overview of the meshed model is presented. The constraints of the model have been set on the two sides of the plate (purple arrow in Fig. 2); in particular, the displacements and rotations of the corresponding nodes in the x, y, and z-axes were constrained. The simulation is a coupled thermal and structural.

The load consisted of a heat input, input by a Goldack model. The volume heat flux is defined for the front part as

$$Q_f(x, y, z, t) = \frac{6\sqrt{3}f_f Q}{abC_f\pi\sqrt{\pi}} \exp \frac{-x^2}{a^2} \exp \frac{-y^2}{b^2} \exp \frac{-z^2}{C_f^2} \quad (2)$$

for the rear part as:

$$Q_r(x, y, z, t) = \frac{6\sqrt{3}f_r Q}{abC_r\pi\sqrt{\pi}} \exp \frac{-x^2}{a^2} \exp \frac{-y^2}{b^2} \exp \frac{-z^2}{C_r^2} \quad (3)$$

where Q is the total heat flux, Q_f and Q_r are the volume heat flux in the front and rear of the double ellipsoidal heat source model, f_1 and f_2 are the fractions of deposition of heat, and $f_1 + f_2 = 2$, while the other parameters are the dimensions of the double ellipsoid.

The material data are taken from the Marc Database, and the steel is a 20MnCr5, as it consists in a multiphase material; the phases are ferrite, pearlite, bainite, martensite, and austenite as S275JR steel is. The thermal and mechanical

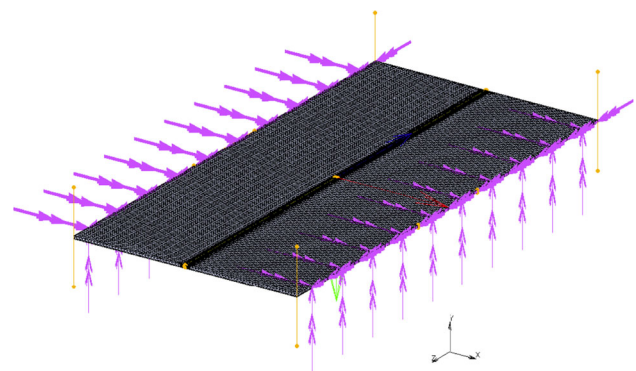


Fig. 2 Meshed model

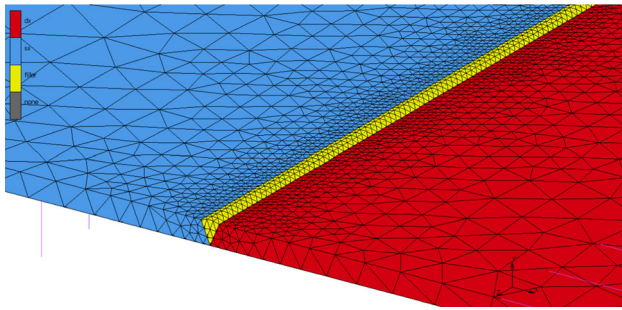


Fig. 3 Detail of weld seam, in yellow, and plates, blue and red, meshed model

phase properties are non-linear. Only the SMAW technique was simulated in order to validate the sound parameter.

The experimental data from the corresponding SMAW butt joint, regarding the thermal temporal cursor, longitudinal profile, section profile, and HAZ dimension, were used to calibrate the Goldack model dimension, while the information regarding current intensity and welding speed, measured experimentally, were used as raw input.

Figure 3 presents a detail of weld seam mesh.

The analyzed outputs of the simulation are temperature data and phase volume fraction.

3 Results

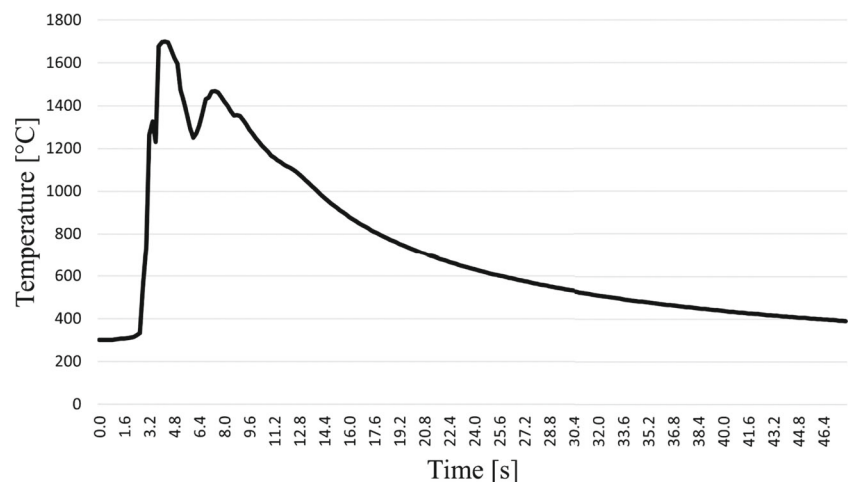
During the experimental activity, different flaws were purposely created in the welded joints, as presented in methodology section. Since some of them are trivial to detect, such as the burn-through, those results are not presented here. For what concerns the lack of penetration, since it is a manual arc welding, it is difficult to find a method to detect it, even if it is relatable to a colder temperature of the weld pool. The most evident flaws related to anomalies in the molten pool are suction pores and improper filling of the groove, adhesion, etc.

due to improper weld parameters. In this section, the results of experimental 3.1 and numerical analysis 3.2 are presented; the aim is to assess what are the *sound parameter* and then, in Section 3.3, to validate the defect detection showing the differences between sound (simulated and experimental) and flaw experimental curves.

3.1 Experimental analysis

In Fig. 4, two examples of C1 curves are reported, in particular the temporal profile of 4 sound areas on the same butt welding that is for the same welding parameters. The results acquired from the reference area show a common pattern. The heating profile is characterized by a noisy trend, related to many occurrences and phenomena: the pass, across the acquired linear profile, of the arc, IR reflection of the liquid weld pool, spatter, and fumes as examples. In particular, due to the fact that it is a manual process, it is difficult to obtain repeatable and reliable thermal information when acquiring the weld pool area. This last kind of artifact can be avoided in the case of automatic welding systems. Furthermore, in the heating step of the C1 curve, the extension of the ROI (in this case, 3x3 pixels) can affect the entity of the noise, and the single time-temperature curve can lose information on the generation of flaws in the welding pool, as the involved areas are more significant than the 3x3 ROI. Furthermore, the position where the acquired ROI is selected affects the C1 cooling and heating profiles obtained experimentally. In fact, a ROI at the beginning of the welding is surrounded by a volume of material whose temperature is lower than a ROI that is positioned in a subsequent place of the welding line, which reaches the highest temperature when the whole average temperature is higher. Generally speaking, the C1 time-temperature plot does not allow us to distinguish the different contributions of arc, weld pool, and fumes on the temperature plot. In the Appendix, some examples are

Fig. 4 C1 curve in non-defect zone



provided for interpreting the generation of noise in the C1 time-temperature plot.

The second common trend in the C1 curve consists in an almost constant temperature profile; it corresponds to the isothermal phase transition related to the solidification of the weld pool, while the noisy signal is related to the liquid molten pool. Once the solidification process starts, an isothermal phase before the start of the cooling is present. More comments on this are provided in the [Appendix](#). After solidification, it can be recognized the typical exponential temperature decay which is a characteristic of thermal diffusive phenomena in bulk materials. This cooling profile presents no noise perturbation. The cooling curve gives an indication of the local quality of the joint, as will be later described. Other important pieces of information can be retrieved by comparing C2 and C3 curves for the two different techniques, SMAW and GMAW. The data shown in Fig. 5 are extracted in the point and in the time instant immediately after the solidification of the weld pool for the two joints.

The surface temperature of the SMAW joint appears to be higher than the GMAW one in both C2 and C3 curves. This is probably related to the presence of the slag crust on the surface of the weld bead. The GMAW temperature appears to be lower probably because of the presence of the

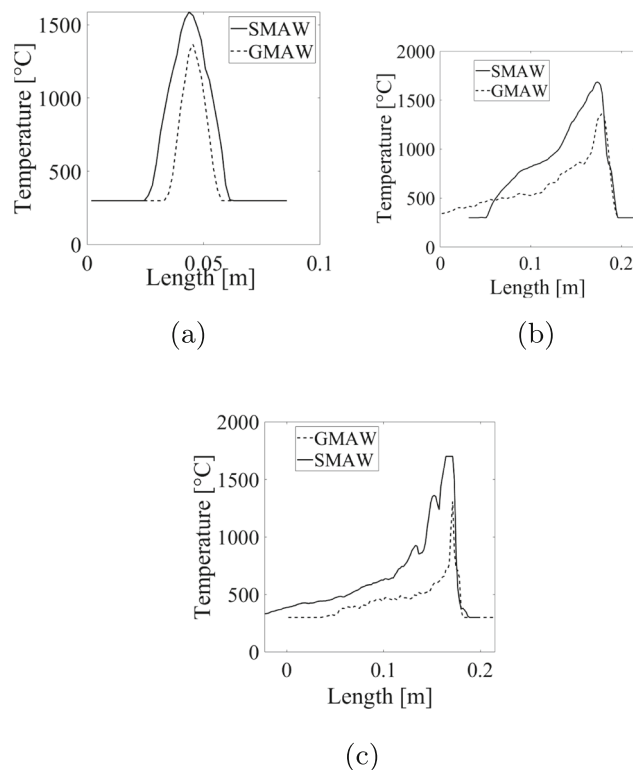


Fig. 5 GMAW [-], SMAW [-], Butt joint C3 curves comparison (a). Butt joint C2 curves comparison (b). Tee joint C2 curve comparison (c)

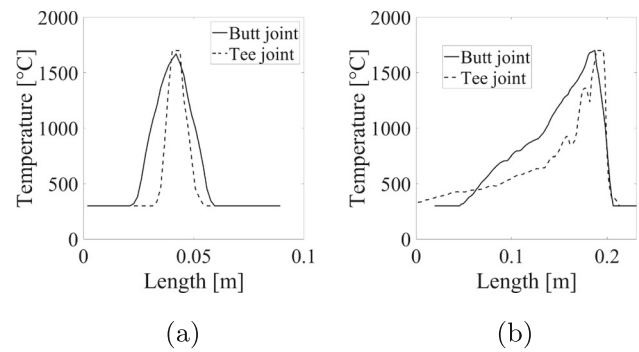


Fig. 6 SMAW butt [-] vs tee [-] joint - C3 curves comparison (a). C2 curves comparison (b)

shielding gas flow during the process interesting insight on this are presented in [53, 54]. The presence of a gas can affect the thermographic temperature measurement due to the gas emissivity effect. In the C2 curves, it is also possible to recognize the waves of the hand movement of the operator in the longitudinal profile of the GMAW. More comments are provided in the [Appendix](#).

Another information relating to the type of shape of the joint is obtained by comparing the C3 curves with the C2 curves as reported in Fig. 6, by comparing a butt joint and a tee joint welded by means of SMAW technique.

In particular, the temperature C2 profile of the tee joint is sharper than the butt joint, due to a larger amount of material able to evacuate the heat of the process than the butt joint. The same phenomenon is observed in the different shape and slope of the tail of the longitudinal profile; the tee joint has a more concave tail than the butt joint.

The C3 curves are important for the HAZ analysis and for calibrating the numerical simulation model. As shown in Fig. 7 for a sound butt SMAW joint as an example, in two-time instants before and after the torch passes by the investigated ROI, it is evident that the experimental temperature C3 curve presents a bell-shape profile which tends to flatten after the welding torch crosses the acquired point. Since this curve represents how far from the weld path the heat diffuses, it is clear that the larger the C3 curve is, the larger the HAZ is.

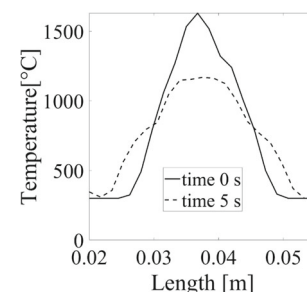


Fig. 7 C3 curves at $t=0$ s [-] and $t=5$ s [-] for sound butt SMAW joint

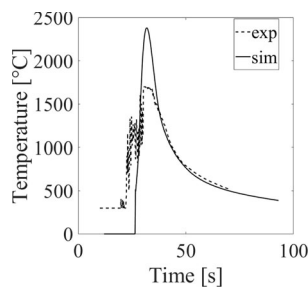


Fig. 8 C1 curves simulation [-] vs experimental [-], butt joint SMAW weld

The experimental data were used as input for the numerical simulation.

3.2 FE Analysis

Entering the numerical results section of our study, it is essential to underscore the significance of using simulation in our approach. The primary objective of our simulation is to define the “sound” parameter, which is a critical element in the process of defect detection. The “sound” parameter represents the thermal behavior of a defect-free or “sound” welding process. Defects, when present, are expected to exhibit a different thermal transient compared to this “sound” curve. This difference is what enables the detection of defects during the welding process. By accurately simulating the “sound” welding process and comparing it with actual experimental curves, we can identify deviations that signal the presence of defects. This method of defect detection is not only efficient but also allows for real-time monitoring, making it a valuable tool in enhancing the quality and reliability of welding processes.

Figure 8 illustrates a comparison between the results derived from the simulation and the experimental data, specifically focusing on the C1 curves for sound regions in butt welds. Notably, the simulated temperature curve achieves higher temperatures and lacks a constant temperature profile. This discrepancy is attributed to the numerical solver’s inability to simulate the phase transition associated with liquefaction and solidification (melting limit). As a result, the numerical simulation heating flux, which is based

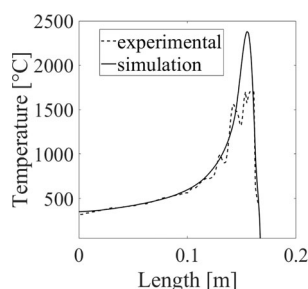


Fig. 9 C2 curves simulation [-] vs experimental [-]

Table 4 HAZ extension in the zone close to the surface

Simulated HAZ	Experimental SMAW HAZ	Experimental GMAW HAZ
23 mm	20.7mm	15 mm

on the Goldack model, continues to elevate the temperature of the material.

Despite these variations and the presence of experimental noise during the heating phase, the heating and cooling profiles are accurately simulated in terms of trend, slope, and time plot. These C1 curves can be employed to calibrate the numerical models, such as using the cooling profile to estimate the heat transmission rate. Subsequently, validation can be achieved by, for instance, C2 curves as depicted in Fig. 9.

The C2 curves depict the heat transmission behavior of the material volume both ahead and behind the heat flux. The heat flow moves towards the colder material volume, resulting in a steep pixel-temperature slope, while the material volume behind the heat front is warmer, leading to a less steep pixel-temperature slope. A meticulous calibration of the thermal physical constitutive model can yield a reliable simulation, as demonstrated in this study. Thermal diffusivity properties are influenced by the material phase distribution and microstructure. A reliable simulation can generate C2 and C3 curves which, when compared to experimental ones, can provide information not only on the presence of flaws but also on the Heat-Affected Zone (HAZ) extension and the actual phase composition in the welding.

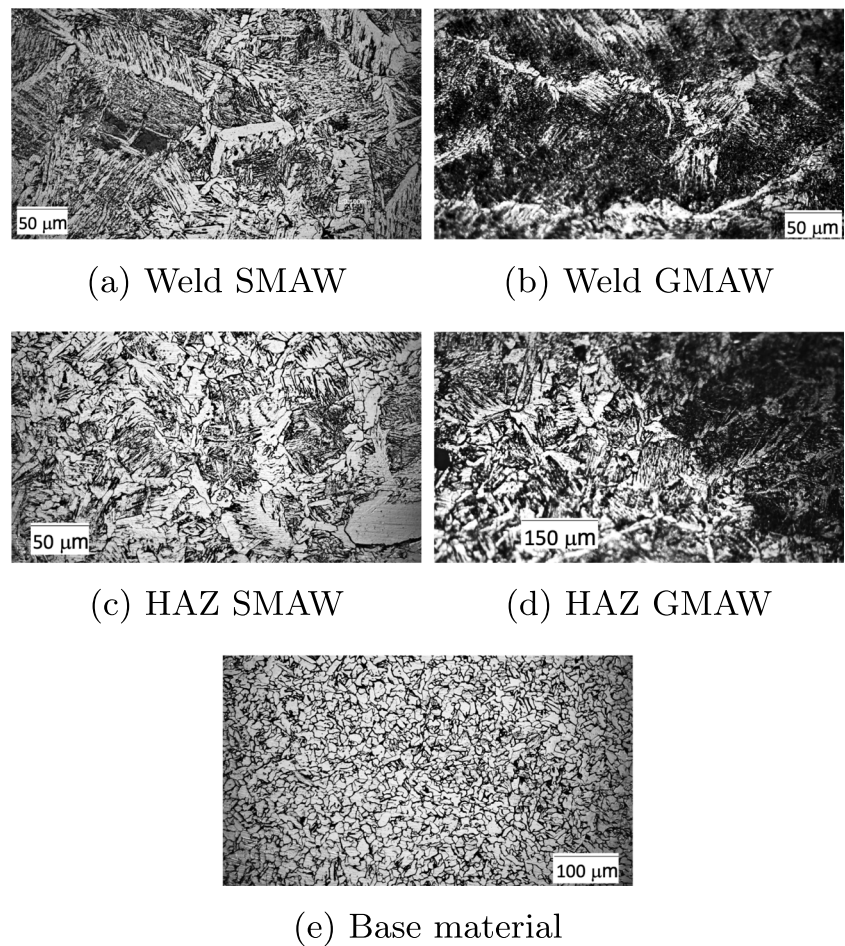
An additional parameter considered for the validation of the numerical model and for the determination of the quality of the joint is the HAZ dimension and metallurgical composition. Then, numerical and experimental results for sound weldings were compared. In Table 4, the comparison between experimental and simulated HAZ is presented.

The simulation of the micrographic composition provided as output in the weld bead a phases fraction, as presented in Table 5

Visual inspection and image analysis of the micrographies of the welded zone, as presented in Fig. 10, allowed to recognize that the microstructure is mostly composed of bainite and martensite, as predicted by the simulation. The two methods, SMAW and GMAW, presented almost the same microstructure in the weld bead and a slightly different transition zone. The differences can be related to the intrinsic

Table 5 Weld bead simulated phase fraction

Martensite	Bainite	Pearlite	Ferrite
40%	50%	3%	7%

Fig. 10 Weld microstructure

differences in the process and to the different compositions of the consumables, such as the cooling rate.

As regards the cooling rate, the slope of C1 curves was used to calculate the cooling rate in the two different techniques as reported in Table 6. The SMAW technique provides a lower heat input which usually tends to facilitate the generation of martensite.

It can be observed that at 900 °C, that is, in the cooling interval after solidification and before phases nucleation, the two slopes are similar, while at 500 °C, immediately before the martensite start temperature, the cooling rate in the SMAW technique is almost half of the GMAW one. This is an additional demonstration that the GMAW cooling transient, because of the lower heat input, leads to a higher martensite phase fraction.

Table 6 Experimental cooling rate in sound butt welds

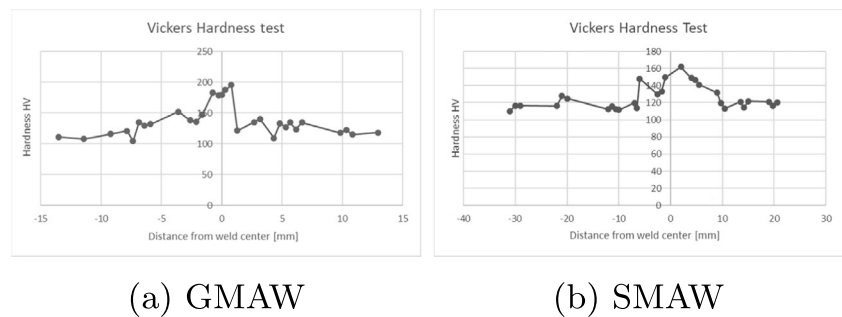
Temperature	SMAW	GMAW
900°C	32 K/s	30 K/s
500°C	7 K/s	12 K/s

A cross-check to validate the HAZ extension estimation is obtained with the hardness test measurements, presented in Fig. 11

The indentation force for the microhardness HV test has been set at 1000 gf. The HV measurements run on the cross-section of the two welded butt joints (SMAW and GMAW) show a HAZ width of about 20 mm for both joints, accordingly to the simulation results. As indicated in Fig. 10, the GMAW weld has a higher percentage of martensite with respect to SMAW, and this has an effect on hardness. In fact, GMAW hardness has a peak of around 200 HV, while the SMAW profile peaks around 160 HV. Microstructure analysis of etched cross-sections confirmed these results.

3.3 Flaws detection

Both experimental and numerical results give an indication on what should be the thermal behavior of a non-defective process, given the welding process parameters configuration. The validation of the model and of the proposed procedure is obtained by comparing the experimental C1, C2, and C3 curves of ROIs where flaws were artificially included with simulated and/or experimental corresponding C1, C2, and

Fig. 11 Hardness profiles

(a) GMAW

(b) SMAW

C3 ones. As an example, in figure (Fig. 12, left), a C3 experimental curve corresponding to a suction pore (dotted line) is presented and compared to the C3 experimental curve of a sound region. The corresponding C2 curves are reported in Fig. 12 (right). In these images, the drop in temperature points out the presence of the defect. As shown in Figs. 22 and 21, the suction pore has a dimension similar to the electrode diameter, so it is possible to state that the thermography can detect pores at least of few millimeters.

Another class of typical welding flaws is generated by arc instabilities. A non-stable arc generates an improper fusion of the consumable electrode and a bad penetration of the welding. This can be detected, for example, by analyzing the longitudinal profile as for example in Fig. 13. It can be observed a very noisy thermal signal along the welding path. There are lower temperatures and several colder temperature drops, while in the case of a correct welding arc, the thermal profile shows a typical trend.

This kind of flaws usually leads to lack of fusion defects and underfilling of the groove. Given the validation of the experimental thermal curves for sound and flaw ROIs, then the simulations in different welding conditions can provide sound thermal contours to be compared with contours to be quality controlled.

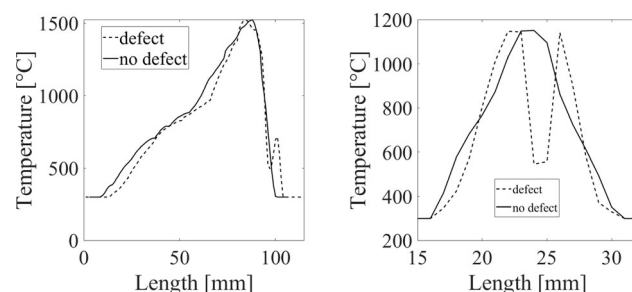
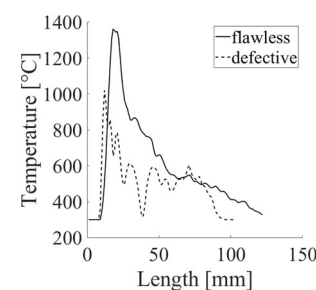
4 Conclusions

In this study, we present a procedure for real-time analysis of the welding process, joint Heat-Affected Zone (HAZ)

extension, phase distribution, and flaw detection using thermographic analysis. Specifically, the proposed technique employs infrared (IR) thermography for the non-destructive evaluation of the weld pool, the acquisition of the cooling transient, and thermal profiles of selected Regions of Interest (ROIs) in low-carbon steel weldings. The analysis primarily focuses on subsurface defects, particularly suction pores.

A numerical model of the welding process and corresponding heat-related phenomena was implemented to obtain the thermal time and space plots on the joint surface, given the welding process parameter configuration. These simulations were calibrated using thermal acquisition obtained during the welding process on sound butt and tee joints made on S275JR laminate steel plates. Subsequently, the thermal profiles obtained on defective welded joints were compared with simulated and experimental sound ones. This comparison revealed that mismatches in the profiles correspond to the presence of a flaw.

The investigation was further extended to the analysis of artifacts in the thermal profiles to provide useful tools for interpreting the results. The thermographic technique was compared with other destructive methods, particularly for the estimation of the HAZ extension. Micrographic analysis was performed to validate experimental thermal profiles and simulation results. A well-executed simulation with correct input parameters, including thermo-physical and mechanical properties of the material, provides reliable space and time temperature curves that reproduce experimental behavior, with the exception of the liquid to solid phase transition.

**Fig. 12** Sound [-] VS defective [-] in C2 (left) and C3 (right) curves**Fig. 13** Wrong parameters effect on C2 curves, correct [-] VS unstable arc [-]

However, it is important to acknowledge the practical challenges and uncertainties associated with this technique. These include the variability of welding conditions, due to manual welding technique, the sensitivity and specificity of the thermal signals, and the scalability and cost-effectiveness of the method. Surely it can have great potential if applied to robotized welding. The use of simulations could be avoided by the use of deep learning algorithms properly trained on large datasets. Future research should address these limitations and explore potential improvements or extensions of the method, such as integrating it with other non-destructive testing techniques or developing automated defect recognition algorithms. Such critical reflection and innovative ideas could enhance the impact and applicability of this study, making it a more valuable contribution to the field of welding process analysis and defect detection.

Appendix

In this section, further comments concerning artifacts in the thermal plots of experimental data and figures are presented.

Figure 14 gives interesting information about a recurrent problem in infrared acquisition. The figure represents the thermogram at the instant immediately after the electrode leaves the weld pool. The molten pool is in liquid phase and the surrounding area in the solid phase. The measured temperature shows a temperature drop (in the red circle) corresponding to the white arrow that is the liquid melt pool. The emissivity of the liquid phase is low, while the reflectivity is elevated. In addition, the signal is really noisy. This is probably related to reflective phenomena due to the liquid metal; after it solidifies, the measured temperature returns to a higher value due to the increased emissivity.

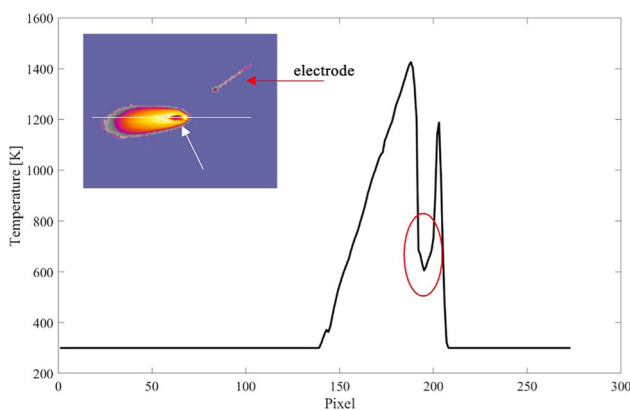


Fig. 14 Weld pool C1 curve

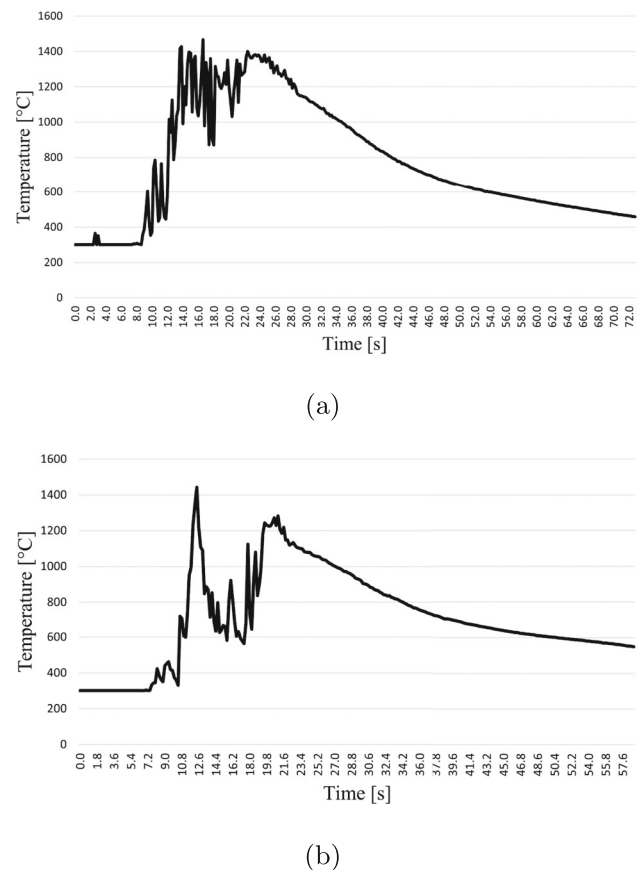


Fig. 15 C1 curves in non-defect zone, particulars

A similar effect is the origin of the noise in the heating profile of C1 curves presented in Fig. 15. The main information is that it is difficult to retrieve consistent data of the heating phase because of the liquid weld pool, the spatter, the arc, the fumes, and the additional degree of complexity related to the electrode movement which obstructs the field of view of the thermal camera (see subfigure (b)).

Since the simulation does describe the phase transition steady temperature corresponding to liquid-to-solid phase change, the simulated temperature profile and the experimental one do not coincide in the molten pool area. In addition, the molten pool area gives unreliable temperature data in the molten pool. To properly validate the simulation, the cooling transient curves (C1) and the C2 and C3 curves are used. Since the thermal phenomena in the welding process are mainly influenced by the thermal diffusion from the bead to the cold lap and by the heat input, this is one of the most important phenomena to be considered validated. In Fig. 16, an example of data used for validation is presented. It is possible to see that the C2 curve gives a wrong measured temperature value in the molten area, as expected, but the

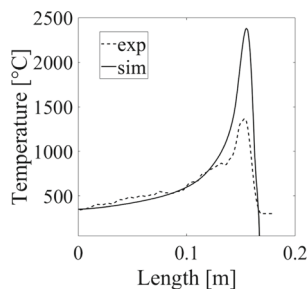


Fig. 16 C2 curve simulation vs experimental 2

tail of the experimental and simulated curves tend to correspond. By slightly changing the simulated input parameter, big mismatches are registered.

Another important aspect that needs to be assessed regarding emissivity is the difference between GMAW and SMAW. In the SMAW technique, immediately after the solidification, the slag creates a crust with high emissivity. Due to

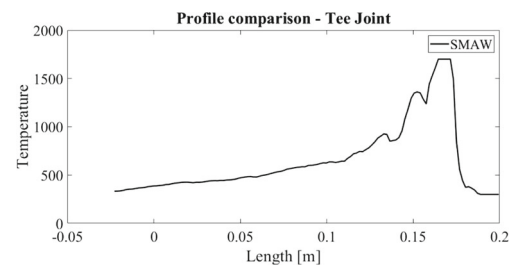
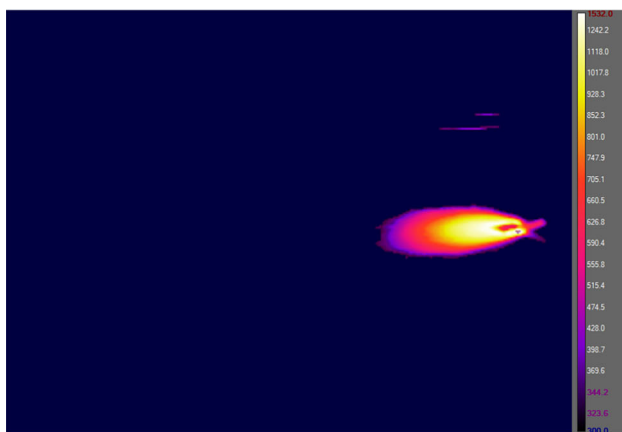


Fig. 18 Waves

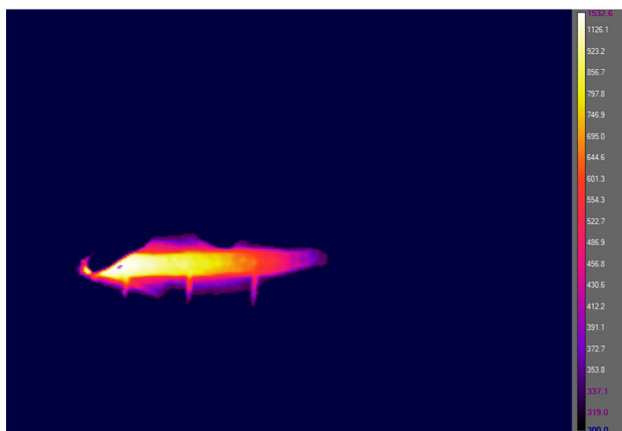
this phenomenon, when calibrating in real time the surface temperature of the welding process in the SMAW technique, the emissivity results to be twice with respect to the GMAW. Another difference between the two process can be made evident when comparing the surface temperature distribution, in particular in the direction perpendicular to the welding direction, as shown in Fig. 17. Given the same temperature range, the area involved in this range is larger for SMAW than for GMAW where it seems that all the heat remains concentrated in the groove zone. This temperature distribution can be related with the extension of HAZ in micrographies, as for example in Fig. 10; in fact, it is possible to see how there is a strong division line between the GMAW's HAZ and molten zone.

Another interesting effect to be interpreted in the experimental acquisition is the wavy trend shown in Fig. 18 corresponding to SMAW bead surface reported in Fig. 19. In this welding technique, the operator moves the torch with a wavy path. The corresponding C2 curve temperature profile can be explained with the local accumulation of heat due to the torch movement, and, on the other hand, since the emissivity is also influenced by the angle of view, then the curved and non-planar irregular bead surface leads to unreliable temperature measurements.

Some dedicated comments about emissivity are required for suction pore detection. As shown in Figs. 20 and 22, the pore is clearly visible as a large temperature drop in the cooling profile of the C2 curve. Actually, the geometry of the



(a) SMAW



(b) GMAW

Fig. 17 SMAW vs GMAW



Fig. 19 SMAW bead surface

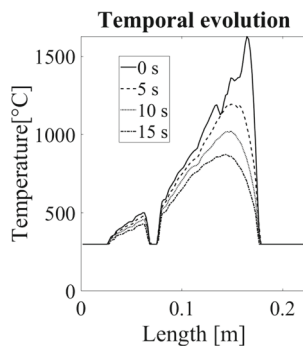


Fig. 20 Temporal evolution of C2 profile at the end of the pass and presence of a suction pore

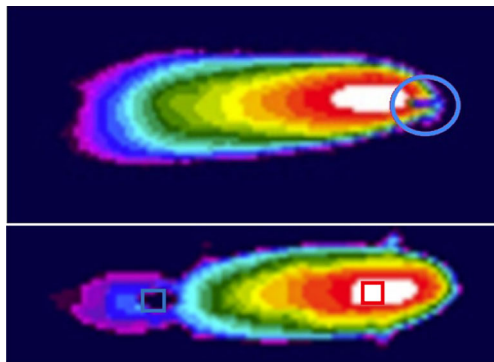


Fig. 21 Suction pore

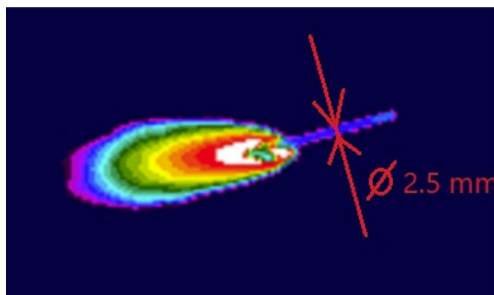


Fig. 22 Electrode diameter

subsurface pore corresponds approximately to an emitting cavity, but due to the geometry of the cavity, the emission in the direction of the camera is not representative of the phenomenon.

Similarly in Fig. 21b, in the thermal contour, the pore is indicated as a colder point, even after the torch is in a subsequent position. In Fig. 21b, the red indication represents the sound region, while the blue one the pore.

In Fig. 22, it is possible to see that the pore has a dimension similar to the electrode diameter.

Funding The authors declare that no funds, grants, or other support were received during the preparation of this manuscript.

Declarations

Conflict of interest The authors declare no competing interests.

Open Access This article is licensed under a Creative Commons Attribution 4.0 International License, which permits use, sharing, adaptation, distribution and reproduction in any medium or format, as long as you give appropriate credit to the original author(s) and the source, provide a link to the Creative Commons licence, and indicate if changes were made. The images or other third party material in this article are included in the article's Creative Commons licence, unless indicated otherwise in a credit line to the material. If material is not included in the article's Creative Commons licence and your intended use is not permitted by statutory regulation or exceeds the permitted use, you will need to obtain permission directly from the copyright holder. To view a copy of this licence, visit <http://creativecommons.org/licenses/by/4.0/>.

References

- Shen J, Agrawal P, Rodrigues TA, Lopes JG, Schell N, Zeng Z, Mishra RS, Oliveira JP (2022) Gas tungsten arc welding of as-cast AlCoCrFeNi_{2.1} eutectic high entropy alloy. *Materials and Design* 223, 111176. <https://doi.org/10.1016/j.matdes.2022.111176>
- Shen J, Gonçalves R, Choi YT, Lopes JG, Yang J, Schell N, Kim HS, Oliveira JP (2022) Microstructure and mechanical properties of gas metal arc welded CoCrFeMnNi joints using a 410 stainless steel filler metal. *Materials Science and Engineering: A* 857:144025. <https://doi.org/10.1016/j.msea.2022.144025>
- Shen J, Gonçalves R, Choi YT, Lopes JG, Yang J, Schell N, Kim HS, Oliveira JP (2023) Microstructure and mechanical properties of gas metal arc welded CoCrFeMnNi joints using a 308 stainless steel filler metal. *Scripta Materialia* 222:115053. <https://doi.org/10.1016/j.scriptamat.2022.115053>
- Ardika RD, Triyono T, Muhyat N (2021) Triyono: A review porosity in aluminum welding. *Procedia Structural Integrity* 33(C), 171–180. <https://doi.org/10.1016/j.prostr.2021.10.021>
- Filyakov AE, Sholokhov MA, Poloskov SI, Melnikov AY (2020) The study of the influence of deviations of the arc energy parameters on the defects formation during automatic welding of pipelines. In: *IOP Conference Series: Materials Science and Engineering*, vol 966. <https://doi.org/10.1088/1757-899X/966/1/012088>
- Hong Y, Yang M, Chang B, Du D (2022) Filter-PCA-based process monitoring and defect identification during climbing helium arc welding process using DE-SVM. *IEEE Transactions on Industrial Electronics*, 1343–1348. <https://doi.org/10.1109/TIE.2022.3201304>
- Nguyen HL, Van Nguyen A, Duy HL, Nguyen T-H, Tashiro S, Tanaka M (2021) Relationship among welding defects with convection and material flow dynamic considering principal forces in plasma arc welding. *Metals* 11(9):1444. <https://doi.org/10.3390/met11091444>
- Zhou Q, Rong Y, Shao X, Jiang P, Gao Z, Cao L (2018) Optimization of laser brazing onto galvanized steel based on ensemble of metamodels. *Journal of Intelligent Manufacturing* 29(7):1417–1431. <https://doi.org/10.1007/s10845-015-1187-5>
- Aucott L, Huang D, Dong HB, Wen SW, Marsden JA, Rack AJ, Cocks ACF (2017) Initiation and growth kinetics of solidification

- cracking during welding of steel. *Scientific Reports* 7. <https://doi.org/10.1038/srep40255>
10. Kalyankar V, Bhoskar A (2021) Influence of torch oscillation on the microstructure of Colmonoy 6 overlay deposition on SS304 substrate with PTA welding process. *Metall Res Technol* 118(4):406. <https://doi.org/10.1051/metal/2021045>
 11. Bhoskar A, Kalyankar V, Deshmukh D (2022) Metallurgical characterisation of multitrack Stellite 6 coating on SS316L substrate. *Canadian Metallurgical Quarterly* 1–13. <https://doi.org/10.1080/00084433.2022.2149009>
 12. Kalyankar V, Bhoskar A, Deshmukh D, Patil S (2022) On the performance of metallurgical behaviour of Stellite 6 cladding deposited on SS316L substrate with PTAW process. *Canadian Metallurgical Quarterly* 61(2), 130–144. <https://doi.org/10.1080/00084433.2022.2031681>
 13. Bang HT, Park S, Jeon H (2020) Defect identification in composite materials via thermography and deep learning techniques. *Composite Structures* 246. <https://doi.org/10.1016/j.compstruct.2020.112405>
 14. Huang J, Pastor ML, Garnier C, Gong XJ (2019) A new model for fatigue life prediction based on infrared thermography and degradation process for CFRP composite laminates. *International Journal of Fatigue* 120:87–95. <https://doi.org/10.1016/j.ijfatigue.2018.11.002>
 15. Pitarresi G, Cappello R, Capraro A, Pinto V, Badagliaccio D, Valenza A (2023) Frequency modulated thermography-NDT of polymer composites by means of human-controlled heat modulation. *Lecture Notes in Civil Engineering* 254 LNCE, 610–618. https://doi.org/10.1007/978-3-031-07258-1_62
 16. Guo X, Vavilov V (2013) Crack detection in aluminum parts by using ultrasound-excited infrared thermography. *Infrared Physics and Technology* 61, 149–156. <https://doi.org/10.1016/j.infrared.2013.08.003>
 17. Park H, Choi M, Park J, Kim W (2014) A study on detection of micro-cracks in the dissimilar metal weld through ultrasound infrared thermography. *Infrared Physics and Technology* 62:124–131. <https://doi.org/10.1016/j.infrared.2013.10.006>
 18. Dell'Ávvocato G, Gohlke D, Palumbo D, Krankenhagen R, Galietti U (2022) Quantitative evaluation of the welded area in Resistance Projection Welded (RPW) thin joints by pulsed laser thermography, p 26. *SPIE-Intl Soc Optical Eng.* ??? <https://doi.org/10.1117/12.2618806>
 19. Dell'Ávvocato G, Palumbo D, Palmieri ME, Galietti U (2022) Non-destructive thermographic method for the assessment of heat treatment in boron steel, p 8. *SPIE-Intl Soc Optical Eng.* ??? <https://doi.org/10.1117/12.2618810>
 20. Cheng Y, Bai L, Yang F, Chen Y, Jiang S, Yin C (2016) Stainless steel weld defect detection using pulsed inductive thermography. *IEEE Transactions on Applied Superconductivity* 26(7). <https://doi.org/10.1109/TASC.2016.2582662>
 21. Yuan B, Spiessberger C, Waag TI (2017) Eddy current thermography imaging for conditionbased maintenance of overlay welded components under multi-degradation. *Marine Structures* 53:136–147. <https://doi.org/10.1016/j.marstruc.2017.02.001>
 22. García de la Yedra A, Fernández E, Beizama A, Fuente R, Echeverría A, Broberg P, Runnemalm A, Henrikson P (2014) Defect detection strategies in Nickel Superalloys welds using active thermography. *QIRT Council*, ??? <https://doi.org/10.21611/qirt.2014.028>
 23. Broberg P (2013) Surface crack detection in welds using thermography. *NDT and E International* 57:69–73. <https://doi.org/10.1016/j.ndteint.2013.03.008>
 24. Li T, Almond DP, Rees DAS (2011) Crack imaging by scanning pulsed laser spot thermography. *NDT and E International* 44(2):216–225. <https://doi.org/10.1016/j.ndteint.2010.08.006>
 25. Schlichting J, Brauser S, Pepke LA, Maierhofer C, Rethmeier M, Kreutzbruck M (2012) Thermographic testing of spot welds. *NDT and E International* 48:23–29. <https://doi.org/10.1016/j.ndteint.2012.02.003>
 26. Maierhofer C, Röllig M, Steinfurth H, Ziegler M, Kreutzbruck M, Scheuerlein C, Heck S (2012) Non-destructive testing of Cu solder connections using active thermography. *NDT and E International* 52:103–111. <https://doi.org/10.1016/j.ndteint.2012.07.010>
 27. Faria JJR, Fonseca LGA, Faria AR, Cantisano A, Cunha TN, Jahed H, Montesano J (2022) Determination of the fatigue behavior of mechanical components through infrared thermography. *Engineering Failure Analysis* 134. <https://doi.org/10.1016/j.engfailanal.2021.106018>
 28. Skibicki D, Lipski A, Pejkowski (2018) Evaluation of plastic strain work and multiaxial fatigue life in CuZn37 alloy by means of the thermography method and energy-based approaches of Ellyin and Garud. *Fatigue and Fracture of Engineering Materials and Structures* 41(12):2541–2556. <https://doi.org/10.1111/ffe.12854>
 29. Curá F, Sesana R (2014) Mechanical and thermal parameters for high-cycle fatigue characterization in commercial steels. *Fatigue and Fracture of Engineering Materials and Structures* 37(8):883–896. <https://doi.org/10.1111/ffe.12151>
 30. Curá F, Gallinatti AE, Sesana R (2012) Dissipative aspects in thermographic methods. *Fatigue and Fracture of Engineering Materials and Structures* 35(12):1133–1147. <https://doi.org/10.1111/j.1460-2695.2012.01701.x>
 31. Naksuk N, Nakgoenthong J, Prinrakoon W, Yuttawiriya R (2020) Real-time temperature measurement using infrared thermography camera and effects on tensile strength and microhardness of hot wire plasma arc welding. *Metals* 10(8):1–14. <https://doi.org/10.3390/met10081046>
 32. Wang Y, Chen Q (2002) On-line quality monitoring in. *Journal of Materials Processing Technology* 120(August 2001):270–274
 33. Vasilev M, Macleod CN, Loukas C, Javadi Y, Vithanage RKW, Lines D, Mohseni E, Pierce SG, Gachagan A (2021) Sensor-enabled multi-robot system for automated welding and in-process ultrasonic NDE. *Sensors* 21(15). <https://doi.org/10.3390/s21155077>
 34. Ma ZX, Cheng PX, Ning J, Zhang LJ, Na SJ (2021) Innovations in monitoring, control and design of laser and laser-arc hybrid welding processes. *MDPI*. <https://doi.org/10.3390/met11121910>
 35. Zhang M, Shu L, Zhou Q, Jiang P, Gong Z (2021) On-line monitoring of penetration state in laser-arc hybrid welding based on keyhole and arc features. In: *Journal of Physics: Conference Series*, vol. 1884. IOP Publishing Ltd, ??? <https://doi.org/10.1088/1742-6596/1884/1/012039>
 36. Huang Y, Yuan Y, Yang L, Wu D, Chen S (2020) Real-time monitoring and control of porosity defects during arc welding of aluminum alloys. *Journal of Materials Processing Technology* 286. <https://doi.org/10.1016/j.jmatprotec.2020.116832>
 37. Hellings MC, Huissoon JP, Kerr HW (1999) Identifying weld pool dynamics for gas metal arc fillet welds. *Science and Technology of Welding and Joining* 4(1):15–20. <https://doi.org/10.1179/stw.1999.4.1.15>
 38. Alfaro SCA, Franco FD (2010) Exploring infrared sensing for real time welding defects monitoring in GTAW. *Sensors* 10(6):5962–5974. <https://doi.org/10.3390/s100605962>
 39. Yun TJ, Oh WB, Lee BR, Son JS, Kim IS (2019) A study on the optimal offset distance between welding torch and the infrared thermometers. *Fluid Dynamics and Materials Processing* 15(1), 1–14. <https://doi.org/10.32604/FDMP.2019.04759>
 40. Speka M, Mattei S, Piloz M, Ilie M (2008) The infrared thermography control of the laser welding of amorphous polymers. *NDT and E International* 41(3):178–183. <https://doi.org/10.1016/j.ndteint.2007.10.005>

41. Mattei S, Grevey D, Mathieu A, Kirchner L (2009) Using infrared thermography in order to compare laser and hybrid (laser+MIG) welding processes. *Optics and Laser Technology* 41(6):665–670. <https://doi.org/10.1016/j.optlastec.2009.02.005>
42. Cao Z, Yang Z, Chen XL (2004) Threedimensional simulation of transient GMA weld pool with free surface. *Welding Journal* (Miami, Fla) 83(6):169–176
43. Zhu C, Cheon J, Tang X, Na SJ, Cui H (2018) Molten pool behaviors and their influences on welding defects in narrow gap GMAW of 5083 Al-alloy. *International Journal of Heat and Mass Transfer* 126:1206–1221. <https://doi.org/10.1016/j.ijheatmasstransfer.2018.05.132>
44. Cho DW, Na SJ, Cho MH, Lee JS (2013) Simulations of weld pool dynamics in V-groove GTA and GMA welding. *Welding in the World* 57(2):223–233. <https://doi.org/10.1007/s40194-012-0017-z>
45. Sebayang D, Manurung YHP, Ariri A, Yahya O, Wahyudi H, Sari AK, Romahadi D (2018) Numerical simulation of distortion and phase transformation in laser welding process using MSC Marc/Mentat. In: *IOP Conference Series: Materials Science and Engineering*, vol 453. <https://doi.org/10.1088/1757-899X/453/1/012020>
46. Ahmad SN, Manurung YH, Mat MF, Minggu Z, Jaffar A, Pruller S, Leitner M (2020) FEM simulation procedure for distortion and residual stress analysis of wire arc additive manufacturing. In: *IOP Conference Series: Materials Science and Engineering*, vol 834. <https://doi.org/10.1088/1757-899X/834/1/012083>
47. Arora H, Singh R, Singh Brar G (2019) Thermal and structural modelling of arc welding processes: a literature review. *Measurement and Control* 52(8):955–969. <https://doi.org/10.1177/0020294019857747>
48. Meng X, Qin G, Su Y, Fu B, Ji Y (2015) Numerical simulation of large spot laser + MIG arc brazing-fusion welding of Al alloy to galvanized steel. *Journal of Materials Processing Technology* 222:307–314. <https://doi.org/10.1016/j.jmatprotec.2015.03.020>
49. EA Brandes, GBB (1992) *Smithells metal reference book*, p 33. Butterworth Heinemann, ???
50. Hagqvist P, Sikström F, Christiansson AK, Lennartson B (2014) Emissivity compensated spectral pyrometry for varying emissivity metallic measurands. *Measurement Science and Technology* 25(2):8. <https://doi.org/10.1088/0957-0233/25/2/025010>
51. British Standard Institution (2019) EN 10025- 4:2019 Standards Publication Hot rolled products of structural steels
52. European Committee for Standardization (2018) EN ISO 6507-1 (2018) Standards Publication Metallic materials - Vickers hardness test
53. Martin AC, Oliveira JP, Fink C (2020) Elemental effects on weld cracking susceptibility in AlxCoCrCuFeNi high-entropy alloy. *Metallurgical and Materials Transactions A: Physical Metallurgy and Materials Science* 51(2):778–787. <https://doi.org/10.1007/s11661-019-05564-8>
54. Shen J, Agrawal P, Rodrigues TA, Lopes JG, Schell N, He J, Zeng Z, Mishra RS, Oliveira JP (2023) Microstructure evolution and mechanical properties in a gas tungsten arc welded Fe42Mn28Co10Cr15Si5 metastable high entropy alloy. *Materials Science and Engineering: A* 867:144722. <https://doi.org/10.1016/j.msea.2023.144722>

Publisher's Note Springer Nature remains neutral with regard to jurisdictional claims in published maps and institutional affiliations.